

Large Eddy Simulation of the flow and heat transfer in a half-corrugated channel with various wave amplitudes

Maryam Mirzaei*, Ahmad Sohankar**, Lars Davidson[†], Fredrik Innings***

*Department of Mechanical Engineering, Yazd University, Yazd, Iran, m.mirzaei@stu.yazduni.ac.ir

[†]Division of Fluid Dynamics, Department of Applied Mechanics,

Chalmers University of Technology, Gothenburg, Sweden, marmir@chalmers.se

**Department of Mechanical Engineering, Isfahan University of Technology, Isfahan, Iran, asohankar@cc.iut.ac.ir

[†]Division of Fluid Dynamics, Department of Applied Mechanics,

Chalmers University of Technology, Gothenberg, Sweden, lada@chalmers.se

***CFD Manager at TetraPak, Lund, Sweden, fredrik.Innings@tetrapak.com

Abstract

Large Eddy Simulation (*LES*) of turbulent flow and convective heat transfer over a half-corrugated channel is presented in this paper. Simulations are performed for various ranges of the normalized wave amplitudes, $AM = 0 - 0.15$ (the ratio of wave height to wave length). The Reynolds number based on the bulk velocity is chosen as $Re_b = 10\,000$ and the Prandtl number is $Pr=0.71$. A comparison between the *DNS* and *LES* results of a plane channel ($AM = 0$) at $Re_\tau = 395$ is also performed. The obtained results indicate that the region of recirculating flow depends strongly on the wave amplitude. This study shows that the Nusselt number (Nu) increases by increasing the wave amplitude until a specific value then it remains approximately constant. The thermal performance parameter (JF) is used as a measure for the heat transfer enhancement relative to the pressure drop and it is found that the maximum values of Nu and JF appear at $AM = 0.1$, which hence correspond to the optimum value of the wave amplitude.

Keywords: Turbulent flow; Large Eddy Simulation (*LES*); half-corrugated channel; wave amplitude; optimum value

1 Introduction

Considerable attention on different methods to increase the rates of heat and mass transfer in compact heat exchangers has been reported. One geometry of the flow passage that is simple to fabricate and has been extensively used to enhance the heat exchanger performance is known as wavy (corrugated) walls. Wavy walls are recognized as effective devices to provide significant heat transfer enhancement. The corrugated channels can be considered to be fully-corrugated

(fully-waved or sinusoidal) or half-corrugated channels. In a fully-corrugated channel, the corrugation is applied to the entire channel length whereas, in a half-corrugated channel, part of the channel becomes corrugated and a part remains smooth (see figure 1). The half-corrugated channel (or wavy channel) is chosen as the configuration under consideration in this work.

A number of numerical and experimental investigations have been reported on turbulent flow over fully-corrugated walls with different wave amplitudes (the ratio of the wave height to wave length, AM) [1]-[6]. Hudson et al. [1] provided extensive measurements of the turbulent characteristics such as the Reynolds stresses, turbulent intensities and production over a fully-corrugated wall with a wave amplitude equal to $AM = 0.05$ and a Reynolds number of 6 760 based on the bulk velocity (u_b) and the mean height of the channel (H). They showed that the turbulence production near the wavy surface is mainly associated with the shear layer separated from the wavy surface. In 1998, Cherukat et al. [2] presented a comprehensive numerical simulation of turbulent flow over a sinusoidal wavy surface by Direct Numerical Simulation (*DNS*) using a spectral element technique. In their simulation they chose the wave amplitude as 0.05 and Reynolds number based on bulk flow velocity and half of the channel height ($H/2$) as $Re_b = 3\,450$. They presented both instantaneous and mean flow results for various characteristics. The instantaneous results showed a large variation of flow pattern in the spanwise direction in the separated bubble at any given time and both the separation and reattachment points varied in time and space. Different turbulent parameters such as turbulence shear stress and turbulence intensities were provided in their studies and a good agreement with the experimental results of Hudson et al. [1] was reported. Tseng et al. (2003) [3], Choi et al. (2005) [4], Pham et al. (2008) [5], Asai (2006) [6] and Chang (2009) [7] conducted numerical and experimental results over the wavy channel. In all studies mentioned above only one wave amplitude was considered.

Some investigations were also reported for wavy channels with different wave amplitudes. Calhoun et al. (2001) [8], Dellil et al. (2004) [9] and Yoon et al. (2009) [10] performed numerical investigations of the effect of the wave amplitude in a fully wavy channel. Calhoun et al. [8] provided a Large eddy Simulation (*LES*) of the flow in a wavy channel. In this study they compared the effects of three different wave amplitudes, $AM = 0.025, 0.05$ and 0.1 at the Reynolds number 7 000. Turbulence statistics and turbulent kinetic energy (*TKE*) budgets showed the locations and magnitudes of the peak values of the statistics. Their results indicated that dissipation, production and transport are the dominant components of the *TKE* budget, but viscous diffusion and pressure diffusion may be significant at some locations. The region over the centre of the wave (maximum channel height) is highly turbulent; peak turbulence intensities, shear stresses, and mean *TKE* are all found in this region. However, in their investigation they only concentrated on the flow field and no result was presented for the thermal field. Dellil et al. [9] reported numerical simulation of turbulent flow and convective heat transfer over a wavy wall using a $k - \epsilon$ model. Their results were provided for wave amplitudes which varied from 0 to 0.1 by a step of 0.02 and at the Reynolds number 6 760. Comparison of the predicted results of a wavy wall with that of a straight channel showed that the Nusselt number (Nu) increases as the amplitude wave is increased until a critical value is reached. However, this heat transfer enhancement is accompanied by an increase in the pressure drop. Their presented results of the thermal

field were limited to the comparison of global Nusselt number and no discussion was provided for the turbulent heat transfer. Yoon et al. [10] investigated numerically the characteristics of three-dimensional turbulent flow in a wavy channel. Their numerical simulations were performed for the range of wave amplitude $AM = 0.01 - 0.05$ and at the Reynolds number 6 760. According to their results the reverse flow appears from $AM = 0.03$ for the wave amplitudes considered in their study. The domain of the mean reverse flow depends strongly on the wave amplitude. The friction drag coefficient (C_f) showed an increasing and decreasing behaviour in direct relation to the wave amplitude. Some quantitative information about the flow variables such as the distribution of pressure and shear stress on the wavy wall was also included. However, in this study as well, the results only covered the flow field variations and no result was mentioned on the thermal field.

In a previous study of the authors [11], *LES* and *DNS* have been applied to study the turbulent flow and thermal fields in a wavy channel with a wave amplitude $AM = 0.08$ at two Prandtl numbers, $Pr = 0.71$ and $Pr = 3.5$, and Reynolds number $Re_b = 10\,000$. The results were also compared to the *DNS* results of a plane channel. Special attention was paid to the behaviour of the flow and thermal boundary layers and various turbulent characteristics and their effects on the distribution of the Nusselt number and friction coefficient near the separation and reattachment points. The obtained results revealed that for both $Pr = 0.71$ and $Pr = 3.5$ the maximum value of the Nusselt number appears around the reattachment point, where the thermal boundary layer has its minimum thickness while the magnitude of thermal turbulent production has its minimum. This implies that the effect of the thermal boundary layer thickness on the Nusselt number is more significant than the thermal turbulent fluctuations. It was also shown that the presence of a corrugation in the channel causes different effects near the separation and reattachment points. The reduced magnitude between the left inflow boundary and the separation point is almost the same for both Prandtl numbers and about 40% while, between the reattachment point and the end of the pitch, the increase is 21% and 36% for $Pr = 0.71$ and 3.5, respectively [11].

In almost all of the reported studies, the fully-wavy channel has been considered while the half-wavy channel is chosen in the present study. Moreover, as mentioned before most of the available studies concentrated mainly on the investigation of turbulent flow field whereas the present study pays detailed attention to both turbulent flow and thermal fields. The work being presented covers *LES* of the flow and thermal field over a half-wavy wall with different wave amplitudes in the range of $AM = 0 - 0.15$, $Re_b = 10\,000$. The main emphasis of the presented study is to find the optimum wave amplitude value to provide the best thermal performance. In this work, a comprehensive investigation is provided for the effect of wave amplitude variation on the behaviour of both flow and thermal fields. The global and local distributions of Nusselt number and friction coefficient are compared for different wave amplitudes. The performance factor (JF) defined as the ratio of the heat transfer enhancement over the pressure drop is calculated for each case with the objective of finding an optimum wave height. Furthermore, a detailed study is presented on both velocity and temperature boundary layers near the wavy wall. Special attention is paid to the variation of the thermal boundary layer behaviour near the wall for different wave amplitudes. The results are presented through both the variation

of the temperature profiles along the channel and the contours of the thermal boundary layer. Various contours of flow and thermal turbulent fields such as Reynolds stresses, wall temperature fluctuations and turbulent heat transfer are presented for different wave amplitudes.

The organization of this paper is as follows. Sections 2 and 3 are devoted to presentation of the numerical method, boundary conditions, the turbulence modeling, the computational domain and grid. The description of the results including an analysis of the global, time-averaged and instantaneous results for the wavy channel with different wave amplitudes is provided in section 4. Finally, some conclusions are drawn in section 5.

2 Governing equations and numerical details

The filtered unsteady governing equations for three-dimensional incompressible viscous flow and energy equation are given as follows:

$$\frac{\partial \bar{u}_i}{\partial t} + \frac{\partial(\bar{u}_i \bar{u}_j)}{\partial x_j} = -\frac{1}{\rho} \frac{\partial \bar{P}}{\partial x_i} + \frac{\partial}{\partial x_j} \left[(\nu + \nu_t) \frac{\partial \bar{u}_i}{\partial x_j} \right] + \beta \delta_{1i} \quad (1)$$

$$\frac{\partial \bar{T}}{\partial t} + \frac{\partial(\bar{u}_j \bar{T})}{\partial x_j} = \frac{\partial}{\partial x_j} \left[\left(\frac{\nu}{Pr} + \frac{\nu_t}{Pr_t} \right) \frac{\partial \bar{T}}{\partial x_j} \right] - \gamma \bar{u}_1 \quad (2)$$

In these equations, x_1 , x_2 , x_3 (x , y , z) denote the Cartesian coordinate system, where the x_1 axis is aligned with the flow direction, the x_2 axis is the wall-normal direction and the x_3 axis is the spanwise direction. β and γ are the streamwise pressure gradient and temperature gradient, respectively. The turbulent viscosity, ν_t , is zero in *DNS*.

The boundary conditions for the *DNS* simulation of the plane channel and the *LES* simulation of the wavy channel are as follows. The periodic boundary condition is employed in the streamwise and spanwise directions for the flow and thermal fields and the no-slip condition and uniform heat flux are employed for the lower wall. *LES* is employed for the wavy channel with symmetric boundary condition at the centre of the channel (at $y = H$), whereas *DNS* is used for the plane channel simulating the whole channel. The obtained results show that near the upper boundary of the wavy channel (centre of the channel), the streamlines are uniform and similar to those for the plane channel flow. Hence, it is expected that employing the symmetric boundary condition for the *LES* simulation does not significantly affect the results. It is worth mentioning that, in the present study the *DNS* solution is applied to the plane channel in two cases, (1): the whole channel and using no-slip boundary condition at $y = 2H$, (2): half of the channel and using symmetric boundary condition at $y = H$. Comparing the results, no significant difference was observed between the two cases.

Employing the periodic boundary condition in the streamwise direction for the velocity and temperature requires special modification in the governing equations. The last terms on the right-hand side of equations 1 and 2 represent the streamwise driving pressure gradient (β) and the temperature gradient (γ) in the streamwise direction (x_1), respectively, corresponding to the streamwise periodic boundary condition. To achieve the desired Reynolds number based on

the bulk velocity (Re_b), β is defined based on the flow rate and is modified in each time step. For the constant heat flux (q_w) condition on the wall, γ is obtained based on the inlet and outlet energy balance as $\gamma = q_w / \rho u_{ref} H c_p$, where u_{ref} is the bulk velocity (u_b), ρ is the density, H is half of the channel height and c_p is the specific heat coefficient.

An incompressible finite volume code based on an implicit, fractional step technique with a multigrid pressure Poisson solver and a non-staggered grid arrangement is employed [12]. The second order Crank-Nicolson scheme is used for time discretization. The spatial discretization is based on the second-order central differencing scheme.

The *WALE* model is used as sub-grid model for *LES*. This sub-grid model reads [13]:

$$\nu_{sgs} = (C_\omega \Delta)^2 \frac{(s_{ij}^d s_{ij}^d)^{3/2}}{(\bar{s}_{ij} \bar{s}_{ij})^{5/2} + (s_{ij}^d s_{ij}^d)^{5/4}} \quad (3)$$

$$s_{ij}^d = \frac{1}{2} (\bar{g}_{ij}^2 + \bar{g}_{ji}^2) - \frac{1}{3} \delta_{ij} \bar{g}_{kk}^2, \quad \bar{s}_{ij} = \frac{1}{2} \left(\frac{\partial \bar{u}_i}{\partial x_j} + \frac{\partial \bar{u}_j}{\partial x_i} \right) \quad (4)$$

where s_{ij}^d is the traceless symmetric part of the square of velocity gradient tensor. The constant $C_\omega = 0.325$. The *WALE* sub-grid model is based on the square of the velocity gradient tensor and accounts for the effects of both the strain and the rotation rate of the smallest resolved turbulent fluctuations. There are some advantages reported for this model compared to the classical Smagorinsky formulation [13]. In the *WALE* model, the eddy-viscosity goes naturally to zero in the vicinity of a wall so no damping function is needed to compute wall bounded flows. The model is also invariant to any coordinate translation or rotation and only local information (no test-filtering operation, no knowledge of the closest points in the grid) are needed and hence this sub-grid model is recognized as a suitable *LES* in complex geometries [13].

3 Computational details and grid verification

The physical problem considered in this study is a three-dimensional periodic half-corrugated (wavy) channel. To reduce the computational costs, only one pitch of the domain is regarded as the computational domain. In a previous study by the authors of the wavy channel [11], the use of one and two pitches were compared and it was found that one pitch is sufficient. A three-dimensional schematic view of the problem under consideration is displayed in figure 1. The half of the height of the channel is H , the channel pitch is $L = 3.68H$ and the width of the channel is $W = 0.5H$. Simulations are performed for various values of the wave amplitude (wave height, H_1) to wavelength (L_1) ratio as $AM = H_1/L_1$ in the range of $AM = 0 - 0.15$; the wavelength is equal to half of the channel length ($L_1 = L/2$), see figure 1(a). The shape of the lower wall in the wavy part is given by $y = -(AM \cdot L_1) \exp(-((7x - x_0)^2)/(2\delta^2))$, where $x_0 = 5.907$ and $\delta = 1.8219$. It should be mentioned that the selected geometry is part of the periodic half-corrugated channel used in Tetra Pak. All the solution variables employed in the present study are normalized as follows. All the geometrical lengths are scaled with the half of the channel height (H);

velocities are normalized with the bulk velocity (u_b); the physical time with H/u_b and the temperature is normalized with the bulk temperature (T_b). The bulk velocity and temperature are defined as:

$$u_b(x) = \int \frac{u(x, y) dy}{H} \quad (5)$$

$$T_b(x) = \int \frac{T(x, y) u(x, y) dy}{H u_b(x)} \quad (6)$$

where T and u are the time and spanwise-averaged temperature and velocity in the computational domain, respectively. The Reynolds number based on the bulk flow velocity and channel half-height is $Re_b = u_b H / \nu = 10\,000$, Prandtl numbers is $Pr = 0.71$. The Nusselt number is defined as $Nu = hH/K$, where K is the air thermal conductivity. h is the heat transfer coefficient and is computed as $h = q_w / (T_w(x) - T_b(x))$, where T_w and q_w are the wall temperature and the constant heat flux on the wall, respectively.

Before presenting the results, it is important to find a proper grid resolution. In the previous study of the authors [11] of the wavy channel with wave amplitude ($AM = 0.08$), computations were made for four grid resolutions $170 \times 130 \times 34$, $338 \times 130 \times 34$, $170 \times 198 \times 64$ and $338 \times 130 \times 34$ (with two pitches in x direction) denoted grid 1, grid 2, grid 3 and grid 4, respectively. For all the grids presented, a uniform grid resolution is chosen for both the streamwise and spanwise directions and the y^+ value for the near wall nodes is less than 1. The global Nusselt number (Nu) and friction coefficient (C_f) and also the streamwise distributions of Nu and C_f were compared for these four grids and grid 3 was chosen as the final grid in the present study and in [11]. In the present study, grid 5 with a finer grid resolutions in the wall-normal direction ($170 \times 266 \times 66$) is also employed for the channel with $AM = 0.15$ (the highest wave amplitude). Figures 2 (a) and 2 (b) present the Nusselt number and friction coefficient, respectively for grids 3 and 5. Comparison of the results reveals that grid 3, already chosen for $AM = 0.08$ [11], is fine enough and using a finer grid shows no significant effect on the results. Close agreement is observed in different parts of both figures. The maximum difference between the results is about 4% and 2.5% for Nusselt number and friction coefficient, respectively. The global Nusselt number for grids 3 and 5 are 47.56 and 49.03, respectively, where the difference is about 3.1%. Similarly, the global values of friction coefficient for grids 3 and 5 are 4.696×10^{-3} and 4.775×10^{-3} respectively, where their difference is about 1.7%. Finally, grid 3 is chosen for all the wave amplitudes in the present study. A schematic view of the grid for $AM = 0.1$ is shown in figure 1(b). The normalized time step is chosen as 0.005 which gives a maximum CFL of 0.85.

The other point is about employing the periodic boundary condition in both the x and z directions. The extent of the domain in the streamwise and spanwise directions should be selected sufficiently large that all turbulent scales are accommodated. In the previous study [11], three different channel widths $z = 0.5$, 1 and 1.5 were selected and compared for the wavy channel with $AM = 0.08$. Comparing two-point correlation results at different distances from the wall in three cases, $z = 0.5$ was finally chosen as the width of the channel in [11]. In the present study, $z = 0.5$ is also selected as the width of the channel with

wave amplitudes for $AM=0\text{-}0.1$. However, in the case of $AM = 0.15$ the three-dimensionality effects in the z direction increases. Hence, $z = 1$ (128 cells) and $z = 1.5$ (196 cells) are also examined to find a suitable width for $AM = 0.15$. Figure 3 provides the Nusselt number and friction coefficient distribution in streamwise direction for two channel widths $z = 1$ and $z = 1.5$ for $AM = 0.15$. A close agreement is observed between the results obtained for the two channel widths. As seen, the maximum and minimum values and their locations and also the recirculation lengths are closely reproduced. Thus, $z = 1$ is selected as a suitable width of the wavy channel for $AM = 0.15$.

4 Results and Discussion

4.1 Flow characteristics over the wave with different amplitudes

The streamlines colored by pressure for four different wave amplitudes $AM = 0.02, 0.04, 0.1, 0.15$ are shown in figure 4. At $AM = 0.02$, the streamlines are parallel in almost whole the channel, the height of the corrugation is too small for a separation to occur in this region. As it is also observed in figure 5, the pressure increases in the first part of the wave for increasing wave amplitude. The pressure variation in the streamwise direction causes an adverse pressure gradient in the first part of the wave leading to flow separation and forming a recirculation region (bubble) in the wavy region. The pressure starts to decrease in the second part of the wave and the flow reattaches to the wall. Inspecting both the streamlines and the pressure distributions for different wave amplitudes (figures 4 and 5), it can be seen that the locations of the separation and reattachment points are affected by the variation of the wave amplitude. As the wave amplitude increases, the sharp variation of the pressure in the first part of the wave starts closer to the smooth part of the channel and leads to an earlier flow separation. This also delays the flow reattachment, which closes the recirculating region in the bottom of the wave. At $AM = 0.15$, the recirculating region almost fills the whole wave region. The centre of the bubble, where the pressure reaches its minimum value (corresponding to $x = 0.75, 0.85$ and 0.9 for $AM = 0.04, 0.1$ and 0.15 , respectively, see figure 4), is also gradually moved to the right side for increasing wave amplitude. Considering the streamlines behaviour above the bubble for $AM = 0.1$ and 0.15 , it can be seen that the streamlines stay parallel until part of the wave and then move down towards the reattachment point. For $AM = 0.1$, these parallel streamlines continue until the middle of the wave, while for $AM = 0.15$ continue almost until $x = 1$. Figure 5 shows that the pressure distributions in the streamwise direction are nearly constant over this region. A maximum point is observed in the pressure distribution for all wave amplitudes. This point occurs close to the reattachment region, see figures 4 and 5.

To show the effect of the wave amplitude on the recirculating region length, the locations of the separation and the reattachment points, where the friction coefficient vanishes, are plotted for different wave amplitudes in figure 6. As can be seen, both the separation and reattachment locations are sensitive to the variation of AM . However, the reattachment point shows more sensitivity to the wave amplitude variation than the separation point. The increase of

the recirculation length from $AM = 0.04$ to 0.06 , $AM = 0.06$ to 0.08 , $AM = 0.08$ to 0.1 and $AM = 0.1$ to 0.15 are about 19.9%, 21.5%, 14.8% and 23.6%, respectively, see figure 6. The minimum increase of the recirculating length occurs between $AM = 0.08$ and 0.1 and the maximum increase appears between $AM = 0.1$ and 0.15 . No separation occurs at $AM = 0.02$ (see figure 4).

The effect of the wave amplitude on the local distributions of the friction coefficient and Nusselt number in the wavy part of the channel are shown in figures 7 and 8, respectively. The results are also compared with the *DNS* results of the present study for a plane channel ($AM = 0$). Considering the distributions of C_f in the wavy part of channel with different wave amplitudes (figure 7), it is seen that C_f decreases in the first half of corrugation and increases in the second half for all the cases. The separation and the reattachment points occur in the first and second halves respectively, for all wave amplitudes. It is seen from figure 7 that since the wave amplitude at $AM = 0.02$ is very small, C_f stays positive all over the wave and no separation occurs. Flow separation occurs when the wave amplitude is increased and it is accompanied by an increase in the recirculation length. The local variations of the Nusselt number versus different wave amplitudes are presented in figure 8. For all the wave amplitudes, the minimum and the maximum Nu are located near the separation and the reattachment points, respectively, and as the size of the recirculating region becomes larger with increasing wave amplitude, the difference between the maximum and the minimum Nu increases. As the wave amplitude increases, the minimum values of Nusselt number move upstream, whereas the maximum values move downstream. However, as observed from figure 8, the rate of increasing of the maximum values close to the reattachment is higher than the decrease of the minimum values close to the separation. This reveals a more sensitive variation of Nusselt number around the reattachment point than near the separation point. The maximum values of Nu and C_f are located at nearly the same locations (downstream of the reattachment point) for all the wave amplitudes. Increasing the wave amplitude increases both Nu and C_f around the reattachment point. As it was also discussed by Choi et al. [4], the ejection and sweep type motions (wall-impingement) appear around the reattachment point. These motions provide some upward and wall-ward fluid movements around the reattachment point. They significantly affect the momentum transfer in this area and are expected to highly affect the turbulent parameters and thermal boundary layer thickness around the reattachment point. The increase of wave amplitude intensifies the fluid motions around the reattachment point resulting in much intense rotational flow in this region. It can also increase the flow acceleration after the reattachment point. Regarding the variations of Nu and C_f , it can be noticed that increasing the wave amplitude is more effective for Nu than C_f close to the reattachment point and the rate of the increase for Nu is higher than that for C_f . These points will be discussed more in detail later. Further detailed discussions can also be found in [4] and [11].

To further investigate the effect of the wave amplitude on the global performance of the wavy channel and also to compare the results with similar channel flow without a wave, the performance factor ($JF = (j/j_0)/(C_f/C_{f0})^{1/3}$, where $j = Nu/(RePr^{1/3})$ and index '0' denotes a channel without a wave) is employed. This factor shows a balance between the increased heat transfer and the increased pressure drop due to using a heat enhancement device in a heat exchanger [14]-[16]. When the JF factor becomes higher than 1, such enhance-

ment is profitable. It should be noted that j_0 and C_{f0} correspond to the *LES* results of the present study for the plane channel at $Re_b = 10\,000$. Table 1 provides the global *DNS* results of the present study ($Re_\tau = 395$), the *DNS* results of Kawamura et. al [17] ($Re_\tau = 395$) and the *LES* results of the present study (at two Reynolds numbers $Re_\tau = 395$ and $Re_\tau = 370$, ($Re_b = 10\,000$)) for the plane channel. It should be noted that $Re_b = 10\,000$ was prescribed for $Re_\tau = 370$ through modifying β (Eq. (1)) at each time step. A good agreement is observed between the obtained results. The difference of Nu and C_f for the *DNS* and *LES* results at $Re_\tau = 395$ of the present study is about 3.2% and 1.3%, respectively.

The global values of Nu , C_f , heat transfer enhancement compared to a plane channel (Nu/Nu_0 , Nu_0 Nusselt number of a plane channel) and performance factor (JF) for different wave amplitudes are provided in table 2. Considering table 2, both Nu and C_f increase with the increase of AM up to $AM = 0.1$, but the rate of increase for Nu decreases at $AM \approx 0.06$. The maximum values of Nu (or Nu/Nu_0) and JF appear at $AM = 0.1$ and $AM = 0.08$, respectively. The difference between JF for $AM = 0.1$ and $AM = 0.08$ is very small (1.2 and 1.196). Thus the wavy channel with $AM = 0.1$, which provides higher Nu and Nu/Nu_0 , can be adopted as the optimum wave amplitude. In table 1 the results of the plane channel ($AM = 0$) are presented for both *DNS* results of the present study and the *DNS* results of Kawamura et al. [17] for the plane channel at $Re_\tau = 395$ and as can be seen, a good agreement between the results is obtained. It should be mentioned that $Re_\tau = 395$, based on the friction velocity, is almost equivalent to $Re_b = 13\,000$, based on bulk velocity.

The wall-normal distributions of the velocity for six cross sections are given in figure 9. The positions of the cross sections are displayed in figure 1. At $AM = 0.02$, the streamlines are almost parallel and similar to that in a plane channel, therefore the velocity profiles are the same in different cross sections and close to that for a plane channel. By increasing the wave amplitude the flow separation starts, and a small bubble with recirculating flow (the negative velocity region in figure 9) is formed at the bottom of the wave. As can be observed, the more the wave height increases the more the maximum negative velocity as well as the size of the recirculating region increases. The other point is the effect of the wave amplitude on the boundary layer thickness after the reattachment point. Considering the velocity profiles after the reattachment point for each wave amplitude, two distinct regions can be recognized near the wall, a high gradient region very close to the wall, described as the inner region, and an almost constant gradient region away from the wall that extends to the centre of the channel, described as the outer region. The velocity gradient close to the wall in the inner region is related to the local friction coefficient. Comparison of the velocity profiles at $x = 1.6$ for the four different wave amplitudes shows that the wall-normal velocity gradient (or local friction coefficient) close to the wall increases for increasing wave amplitude, see also figure 7. Thus, the thickness of the inner region decreases for increasing wave amplitude at $x = 1.6$. The thickness of the inner layer at $x = 2$ increases and the velocity gradient (or local friction coefficient) close to the wall decreases compared with that at $x = 1.6$. The interpretation of the relation between the variation of the inner region thickness and the local friction coefficient for the various wave amplitudes can also be extended to the other cross sections.

To further clarify the effect of the wave height on the location of the highly

turbulent content regions, the contours of the turbulent normal stresses ($\langle u'^2 \rangle$, $\langle v'^2 \rangle$, $\langle w'^2 \rangle$), the turbulent shear stress ($\langle u'v' \rangle$) and also the turbulent kinetic energy (k) in the wavy part of the channel are presented in figures 10-15. The black streamlines indicate the boundaries of the recirculating region.

The contours of the turbulent normal (streamwise) stress ($\langle u'^2 \rangle$) for four wave amplitudes are shown in figure 10. A high turbulent region is observed in the shear layer above the recirculating region for all cases. This region starts around the separation point and continues until after the reattachment point. As the height of the wave increases, the size of high turbulent region becomes larger and as can be observed, the size of this region close to the reattachment point is larger than that close to the separation point. For $AM = 0.02, 0.04$ and 0.1 , the maximum value of $\langle u'^2 \rangle$ at the center of the shear layer increases for increasing wave amplitude whereas, for $AM = 0.15$, the maximum value decreases. Figure 11 provides the contours of the turbulent wall-normal stress ($\langle v'^2 \rangle$). By increasing the wave amplitude, a high turbulent region is formed in the second half of the wave. In all cases, the region with high local values is close to the reattachment point and the centre of this region is the reattachment point, which corresponds to wall-normal flow impingement downstream of the reattachment point. Similar to $\langle u'^2 \rangle$, the maximum value of $\langle v'^2 \rangle$ increases for increasing wave height for $AM = 0.02, 0.04$ and 0.1 while for $AM = 0.15$, the maximum value decreases. The contours of the turbulent normal (spanwise) stress $\langle w'^2 \rangle$ are shown in figure 12. Similar to $\langle v'^2 \rangle$, a high local region $\langle w'^2 \rangle$ is formed close to the reattachment point. However, for $\langle w'^2 \rangle$ this high region is narrower and also closer to the reattachment point. Unlike $\langle u'^2 \rangle$ and $\langle v'^2 \rangle$, the maximum value of $\langle w'^2 \rangle$ increases for increasing wave height for all wave amplitudes.

When one compares the maximum values of $\langle u'^2 \rangle$, $\langle v'^2 \rangle$ and $\langle w'^2 \rangle$, it is observed that the largest relative effect of the wave amplitude occurs on $\langle w'^2 \rangle$ and the lowest effect appears on $\langle u'^2 \rangle$. The maximum values of $\langle w'^2 \rangle$ at $AM = 0.02$ and $AM = 0.1$ are about 0.022 and 0.034, respectively, implying an enhancement of about 55% whereas, for $\langle w'^2 \rangle$ the maximum values at $AM = 0.02$ and $AM = 0.15$ are about 0.004 and 0.024, respectively, indicating almost a factor of six.

The contours of the turbulent shear stress ($-\langle u'v' \rangle$) in the wavy part of channel are presented in figure 13. At $AM = 0.02$, no separation occurs on the wall, therefore no shear layer is observed above the wave. By increasing the wave height, the distance between the separation and reattachment points increases. Thus, the size of the recirculating region as well as the separated shear layer become larger and the shear layer continues almost until the end of the channel. Furthermore, by increasing the wave amplitude from $AM = 0.04$ to 0.1 the magnitude of the turbulent shear stress increases, whereas from $AM = 0.1$ to 0.15 , the magnitude decreases. A small negative region close to the wall in the second half of the wave (shown by the black arrows) is observed in figure 13. Hudson et al. [1] observed similar negative regions of the shear stress for the fully wavy channel and mentioned that these negative values will disappear if the shear stress is calculated in a $s - n$ coordinate system aligned with the wavy wall. However, in the previous study of the authors the shear stresses were transformed to the $s - n$ coordinate system and no significant difference was observed [11]. The different terms in the shear stress equation were compared in the negative $-\langle u'v' \rangle$ region and it was concluded that these negative values

are produced by the pressure strain term, which appears as a source term in this region [11]. It should be mentioned that a similar transformation to the $s - n$ coordinate was also performed for various wave amplitudes in the present study and no difference was observed in any of the cases. Furthermore, no negative region of $-\langle u'v' \rangle$ is observed close to the wall at $AM = 0.02$. For higher wave amplitudes, a narrow negative region of $-\langle u'v' \rangle$ is formed close to the wall of the second half of the wave. The size of the positive pressure strain region in the second half of the wave increases for increasing wave amplitude leading to an increased size of the region of negative $-\langle u'v' \rangle$. Thus, it is concluded that the pressure strain is the reason for this region of negative $-\langle u'v' \rangle$ as was also reported in our previous work [11].

Figures 14 and 15 compare $\langle u'^2 \rangle$, $\langle v'^2 \rangle$, $\langle w'^2 \rangle$, $-\langle u'v' \rangle$ and the turbulent kinetic energy (k). The presented results are concentrated to the cross section at the centre of the wave ($x = 0.8$) in figure 14 and close to the reattachment point in figure 15. The same observations can be made as in the contours plots: a maximum value can be seen in both cross sections which correspond to the shear layer above the recirculating region. The variations of $\langle u'^2 \rangle$ and k and also the locations of their maximum points are similar for all wave amplitudes. At the centre of the wave, the maximum values of $\langle v'^2 \rangle$, $\langle w'^2 \rangle$ and $-\langle u'v' \rangle$ are rather close and significantly smaller than those for $\langle u'^2 \rangle$ and k , while around the reattachment point, the maximum values are more close to each other. By increasing the height of the wave, the size of the recirculating region becomes larger, which pushes the separated shear layer away from the wall, and thus the location of the maximum values also moves away from the wall. The *DNS* results of the present study for the plane channel are also presented in figures 14 (a) and 15 (a). As can be observed, at $x = 0.8$ the results of $\langle u'^2 \rangle$, $\langle v'^2 \rangle$ and $\langle w'^2 \rangle$ for the plane channel ($AM = 0$) and $AM = 0.02$ are quite similar, whereas at $x = 1.2$ the maximum values of $\langle u'^2 \rangle$ for $AM = 0$ is much smaller than that for $AM = 0.02$. The maximum value of $\langle u'^2 \rangle$ increases by increasing the wave amplitude, except for the largest wave amplitude. Comparing the dominating part of the production of $\langle u'^2 \rangle$, $-2\langle u'_1 u'_2 \rangle \frac{\partial \langle \bar{u}_1 \rangle}{\partial x_2}$, for different wave amplitudes in figure 16, it can be observed that the production in the shear layer increases by increasing the wave amplitude to $AM = 0.1$, then it decreases for $AM = 0.15$. This explains the variation of $\langle u'^2 \rangle$ with wave amplitude.

4.2 The effect of the wave amplitude on the thermal field:

Figure 17 presents the wall-normal distributions of the temperature for six different cross sections in the streamwise direction. The cross sections are shown in figure 1. The results are compared with the *DNS* results of the present study and also the *DNS* results of Kawamura et al. [17] for the plane channel flow. Comparing the *DNS* results of the present study with the *DNS* results of [17], a good agreement is observed indicating the accuracy of the obtained results of the present study. Similar to what was described for the velocity distributions, two distinct thermal regions appear in the temperature distributions: one high gradient region close to the wall, i.e. the thermal inner region, and one almost constant gradient region, i.e. the thermal outer region (see figure 17). At $AM = 0.02$, the form of the temperature profiles are similar for all the cross sections and also close to that for a plane channel flow. The maximum thickness of the thermal inner layer appears around the centre of the wave ($x \simeq 0.8$)

and downstream of this point the thickness is almost constant. For the three other wave amplitudes, the maximum thickness of the thermal inner layer is around the separation point and the minimum thickness is close to the reattachment point. Comparison of the effect of the wave amplitude for the results around the reattachment and separation points shows that the variation of the thermal inner layer thickness with wave amplitude close to the reattachment point is more significant than that around the separation point. For example, at $x = 0.4$ (close to the separation point) the thickness of the thermal inner layer is almost the same for three cases $AM = 0.04, 0.1$ and 0.15 , whereas at $x = 1.2$ and $x = 1.6$ (close to the reattachment point) the thickness of inner layer is smaller for $AM = 0.15$ than for $AM = 0.1$. As can be observed from the Nusselt number distributions for different wave amplitudes (figure 8), the variation of Nu with wave amplitude around the separation and reattachment points are similar to the variations of the thermal inner layer thickness in these regions. The Nusselt number enhancement around the reattachment point is higher than the reduction around the separation point. Except for $AM = 0.15$, the Nusselt number value around the separation point is almost the same.

As was mentioned in [11], the location of the thermal boundary layer edge can be determined by $\delta_T = (T - T_w)/(T_b - T_w)$, where T_w and T_b represent the wall and bulk temperatures, respectively. According to this formula, $\delta_T = 0$ and $\delta_T = 1$ correspond to the locations of the wall and the boundary layer edge, respectively. The contours of δ_T in the near wall region of the wavy channel are presented in figure 18. In all cases, the maximum thickness of the thermal boundary layer appears around the separation point and the minimum thickness occurs close to the reattachment point and they correspond to the maximum and minimum locations of the Nusselt numbers, see figure 8. As can be seen, the thickness of the thermal boundary layer around the separation point increases slightly for increasing wave amplitude. The location of the maximum thickness moves a bit upstream for increasing wave amplitude due to the variation of separation point. On the other hand, the thickness of thermal boundary layer around the reattachment point decreases slightly for increasing wave amplitude.

Figure 19 presents the contours of the temperature fluctuation, t_{rms} , (left side) and wall-normal turbulent heat transfer, $\langle v't' \rangle$, (right side). Comparison of the contours $\langle v't' \rangle$ in figure 19 indicates that for the three wave amplitudes $AM = 0.04, 0.1$ and 0.15 , the maximum values of $\langle v't' \rangle$ appear in the shear layer region. The maximum value of $\langle v't' \rangle$ for three cases are almost the same and about 0.018 showing that increasing the wave amplitude has no significant effect on the maximum values of $\langle v't' \rangle$. Considering the temperature fluctuations contours, the high local values of t_{rms} appear around the separation point. For $AM = 0.1$ and $AM = 0.15$ there are two regions of large fluctuations, one is close to the separation point and one is between the separation point and the centre of the wave. Figure 20 compares the streamwise distribution of t_{rms} at the wall for different wave amplitudes and as can be observed, except for the channel with $AM = 0.02$, two distinct maximum points can be recognized. The first maximum point is around the separation point and it moves to the left side by increasing the wave amplitude. The second one is rather close to the centre of the wave and its location is almost similar for all the wave amplitudes.

5 Conclusion

The present study numerically investigates the characteristics of three-dimensional turbulent flow in a wavy channel. The numerical simulations are performed for various values of wave amplitudes in the range of $AM = 0 - 0.15$. Large Eddy Simulation (*LES*) is employed as simulation tool. The Reynolds number based on the bulk velocity is $Re_b = 10\,000$ and the Prandtl number is 0.71. Direct Numerical simulation (*DNS*) is also applied for a plane channel ($AM = 0$) at $Re_\tau = 395$. The following conclusions are drawn.

1. The maximum values of Nu and JF appear at $AM = 0.1$ and $AM = 0.08$, respectively. The difference between JF for $AM = 0.08$ and $AM = 0.1$ is very small. Thus $AM = 0.1$ is selected as the optimum wave amplitude to provide the best thermal performance.
2. Up to $AM = 0.02$, no separation occurs in the wave region. For higher wave amplitudes, an adverse pressure gradient in the first part of the wave leads to the flow separation and forms a recirculation region in the wavy part. The pressure starts to decrease in the second part of the wave and the flow reattaches to the wall. The size of the recirculation region becomes larger for higher AM .
3. The separation and reattachment locations are both sensitive to the variation of wave amplitude (AM). However, the reattachment point shows more sensitivity to AM variation than the separation point.
4. The thickness of the inner flow region after the reattachment point decreases for increasing wave amplitude corresponding to the decrease of the friction coefficient at the region.
5. As the height of the wave increases, the size of highly turbulent region becomes larger and the size of this region close to the reattachment point is larger than that close to the separation point.
6. The variation of the thermal inner layer thickness close to the reattachment point is more significant than that around the separation point. For all the wave amplitudes, the maximum thickness of the thermal boundary layer appears around the separation point and the minimum thickness occurs close to the reattachment point corresponding to the minimum and maximum locations of the Nusselt numbers.

Acknowledgment

This work was carried out at Chalmers during a one-year research visit of the first author.

References

- [1] J. D. Hudson, L. Dykhno, T. J. Hanratty, Turbulence production in flow over a wavy wall, *Int. J. Experiments in Fluids*, vol. 20, pp. 257-265, 1996.

- [2] P. Cherukat, Y. Na, and T.J. Hanratty, Direct numerical simulation of a fully developed turbulent flow over a wavy wall, *J. Theoretical and Computational Fluid Dynamics*, vol. 11, pp. 109-134, 1998.
- [3] Y. H. Tseng and J. H. Ferziger, Large-eddy simulation of turbulent wavy boundary flow illustration of vortex dynamics, *J. Turbulence*, vol. 5, pp. 775-789, 2004.
- [4] H. S. Choi, K. Suzuki, Large eddy simulation of turbulent flow and heat transfer in a channel with one wavy wall, *Int. J. Heat and Fluid Flow*, vol. 26, pp.681-694, 2005.
- [5] M.V. Pham, F. Plourde, S.K. Doan, Turbulent heat and mass transfer in sinusoidal wavy channels, *Int. J. Heat and Fluid Flow*, vol. 29, pp. 1240-1257, 2008.
- [6] M. Asai, J.M. Floryan, Experiments on the linear instability of flow in a wavy channel, *European J. Mechanics B/Fluids*, vol. 25, pp. 971-986, 2006.
- [7] S. W. Chang, A. W. Lees, T. C. Chou, Heat transfer and pressure drop in furrowed channels with transverse and skewed sinusoidal wavy walls, *Int. J. Heat and Mass Transfer*, vol. 52, pp. 4592-4603, 2009.
- [8] R. J. Calhoun and R. L. Street, Turbulent flow over a wavy surface: Neutral case, *J. Geophysical Research*, vol. 106, pp. 9277-9293, 2001.
- [9] A. Z. Dellil, A. Azzi, B. A. Jubran, Turbulent flow and convective heat transfer in a wavy wall channel, *Int. J. Heat and Mass Transfer*, vol. 40, pp. 793-799, 2004.
- [10] H. S. Yoon, O. A. El-Samni, A. T. Huynh, H. H. Chun, H. H. Kim, A. H. Pham, I. R. Park, Effect of wave amplitude on turbulent flow in a wavy channel by direct numerical simulation, *Int. J. Ocean Engineering*, vol. 36, pp. 697-707, 2009.
- [11] M. Mirzaei, L. Davidson, A. Sohankar, F. Innings, The effect of corrugation on heat transfer and pressure drop in channel flow with different Prandtl numbers, *Int. J. of Heat and Mass transfer*, vol. 66, pp. 164-176, 2013.
- [12] L. Davidson and S. H. Peng, Hybrid LES-RANS: A one-equation SGS model combined with a $k - \omega$ for predicting recirculating flows, *Int. J. Numerical Methods in Fluids*, vol. 43, pp. 1003-1018, 2003.
- [13] F. Nicoud and F. Ducros, Subgrid scale stress modeling based on the square of the velocity gradient tensor, *Int. J. Flow, Turbulence and Combustion*, vol. 62, pp. 183-200, 1999.
- [14] F. Ke, L. B. Wang, L. Hua, S. D. Gao, and Y. X. Su, The optimum angle of attack of delta winglet vortex generator on heat transfer performance of finned flat tube bank with considering nonuniform fin temperature, *Experimental Heat Transfer*, vol. 19, pp.227-249, 2006.
- [15] A. Sohankar, Heat transfer augmentation in a rectangular channel with a vee-shaped vortex generator, *Int. J. Heat and fluid flow*, vol. 28, pp. 306-317, 2007.

- [16] M. Mirzaei and A. Sohankar, Heat transfer augmentation in plate finned tube heat exchangers with vortex generators: A comparison of round and flat tubes, IJST, Transactions of Mechanical Engineering vol. 37, No. M1, pp 39-51, 2013.
- [17] H. Kawamura, H. Abe and K. Shingai, DNS of turbulence and heat transport in a channel flow with different Reynolds and Prandtl numbers and boundary conditions, 3rd Int. Symp. on Turbulence, Heat and Mass Transfer, Japan, 2000.

6 Tables

	Nu	C_f
<i>DNS</i> present study, $Re_\tau = 395$	37.9	3.05×10^{-3}
<i>DNS</i> Kawamura et. al [17], $Re_\tau = 395$	37.5	3.195×10^{-3}
<i>LES</i> present study, $Re_\tau = 395$	39.12	3.01×10^{-3}
<i>LES</i> present study, $Re_b = 10000$ ($Re_\tau = 370$)	35.2	2.78×10^{-3}

Table 1: *DNS* and *LES* results of the global averaged Nusselt number (Nu) and friction coefficient (C_f) for the plane channel

	Nu	Nu/Nu_0	C_f	JF
$AM = 0.02$	39.62	1.125	3.476×10^{-3}	1.045
$AM = 0.04$	41.58	1.181	4.174×10^{-3}	1.032
$AM = 0.06$	47.6	1.352	4.206×10^{-3}	1.178
$AM = 0.08$	48.8	1.386	4.284×10^{-3}	1.200
$AM = 0.1$	49.42	1.404	4.502×10^{-3}	1.196
$AM = 0.15$	47.56	1.351	4.696×10^{-3}	1.179

Table 2: Global averaged Nusselt number (Nu), Nusselt number ratio (Nu/Nu_0 , Nu_0 Nusselt number of a plane channel), friction coefficient (C_f) and performance factor (JF) for different wave amplitudes

7 Figures

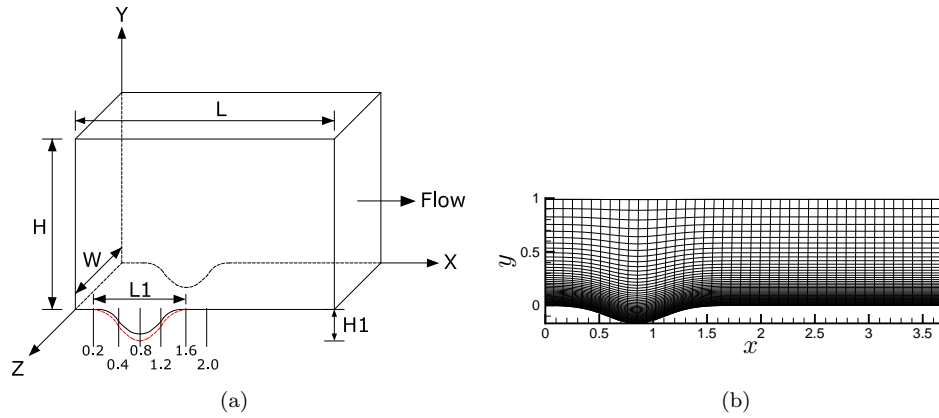


Figure 1: (a). A schematic three-dimensional view of computational domain with two different wave amplitudes ($AM = H_1/L_1$, $L_1/L = 0.5$), (b). grid resolution on a xy -plane in the wavy part of the channel ($AM = 0.1$)

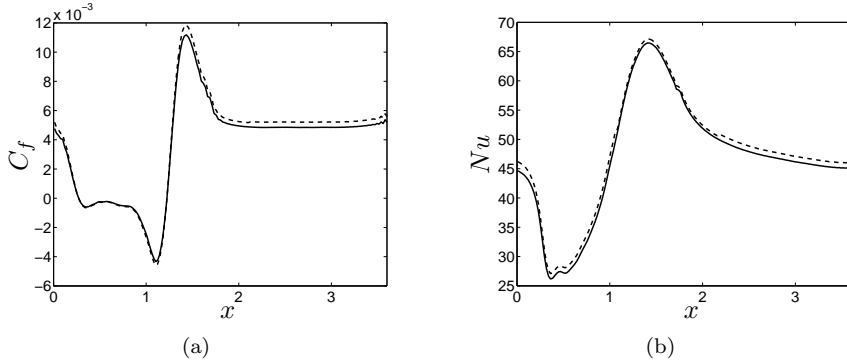


Figure 2: Streamwise distribution of time and spanwise averaged (a). Friction coefficient (C_f) and (b). Nusselt number (Nu) at $AM = 0.15$, - - - : grid 3; — : grid 5

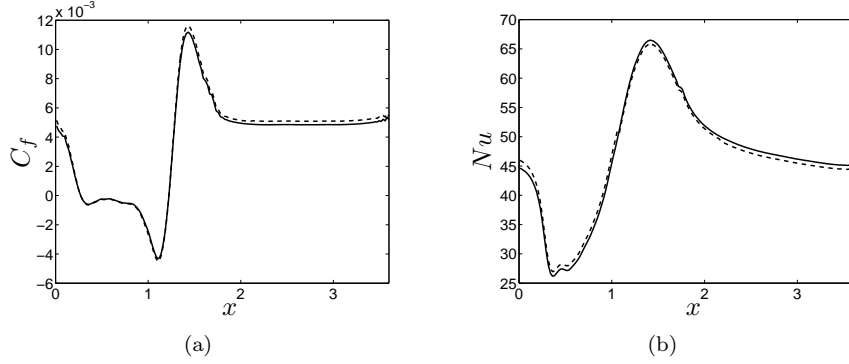


Figure 3: Streamwise distribution of time and spanwise averaged (a). Friction coefficient (C_f) and (b). Nusselt number (Nu) in the wavy channel at $AM = 0.15$ for two channel widths, $- - -$: $z = 1, 128$ cells; $- -$: $z = 1.5, 196$ cells.

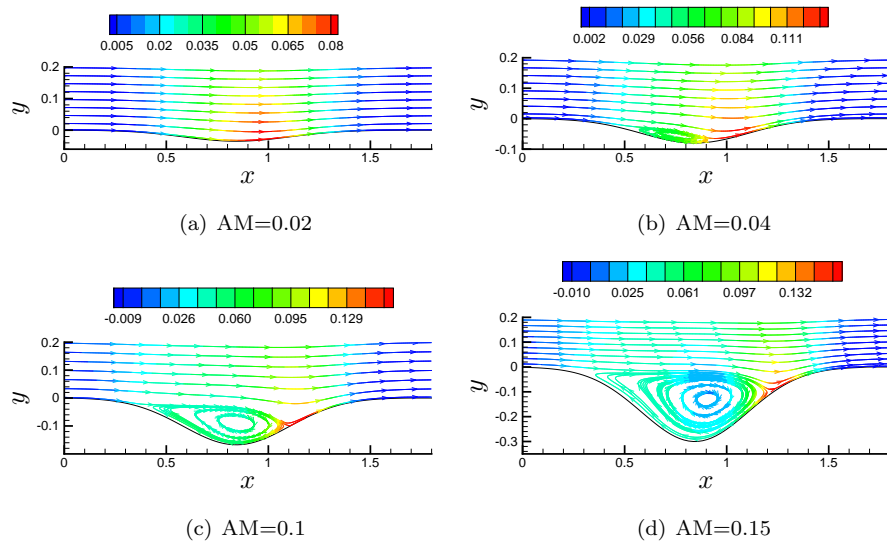


Figure 4: Time and spanwise-averaged streamlines colored by pressure in the wavy part of the channel with four different wave amplitudes $AM = 0.02, 0.04, 0.1, 0.15$

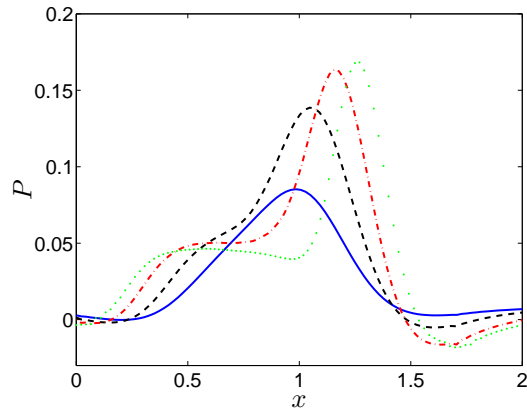


Figure 5: Time and cross-section averaged pressure distribution in the wavy part of the channel for various wave amplitudes, — : $AM = 0.02$; - - : $AM = 0.04$; - - - : $AM = 0.1$; ··· : $AM = 0.15$

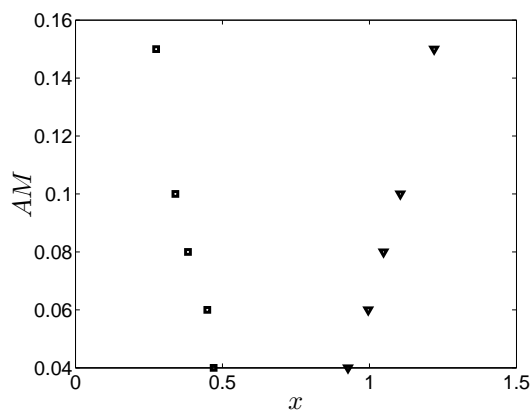


Figure 6: The locations of the separation and reattachment points for different wave amplitudes, ■: separation; ▼: reattachment

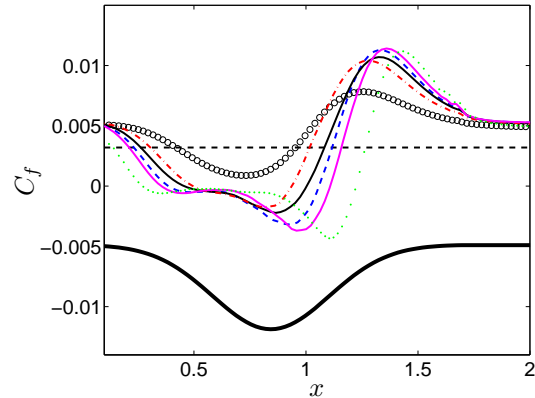


Figure 7: Streamwise distributions of the time and spanwise averaged friction coefficient (C_f) in the wavy part of the channel for different wave amplitudes (AM). The thick black line in the lower part of the figure shows the contour of the wall for $AM = 0.1$; $--$: $AM = 0$; \circ : $AM = 0.02$; $-.$: $AM = 0.04$; $-$: $AM = 0.06$; $-.$: $AM = 0.08$; $-$: $AM = 0.1$; $-.$: $AM = 0.15$

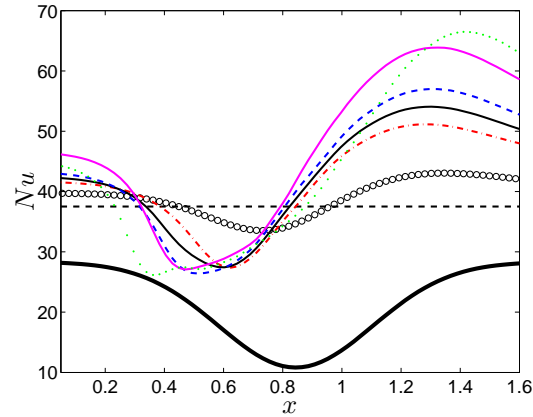


Figure 8: Streamwise distributions of the time and spanwise averaged Nusselt number (Nu) in the wavy part of the channel for different wave amplitudes (AM). The thick black line in the lower part of the figure shows the contour of the wall for $AM = 0.1$, \cdots : $AM = 0$; \circ : $AM = 0.02$; --- : $AM = 0.04$; — : $AM = 0.06$; --- : $AM = 0.08$; — : $AM = 0.1$; --- : $AM = 0.15$

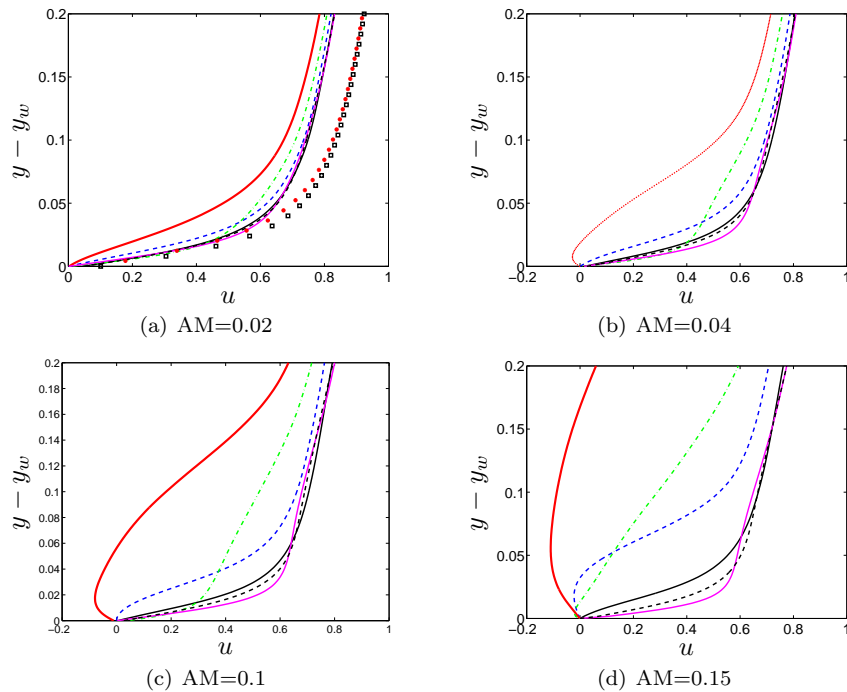


Figure 9: Wall-normal distributions of the time and spanwise averaged velocity at six cross sections for different wave amplitudes (AM). Cross sections are shown in figure 1, — : $x = 0.2$; - - - : $x = 0.4$; — : $x = 0.8$; - - - : $x = 1.2$; — : $x = 1.6$; - - - : $x = 2$; \square : ... : DNS present study. y_w : the normal distance of the wavy wall surface respect to the xz -plane, see figure 1.

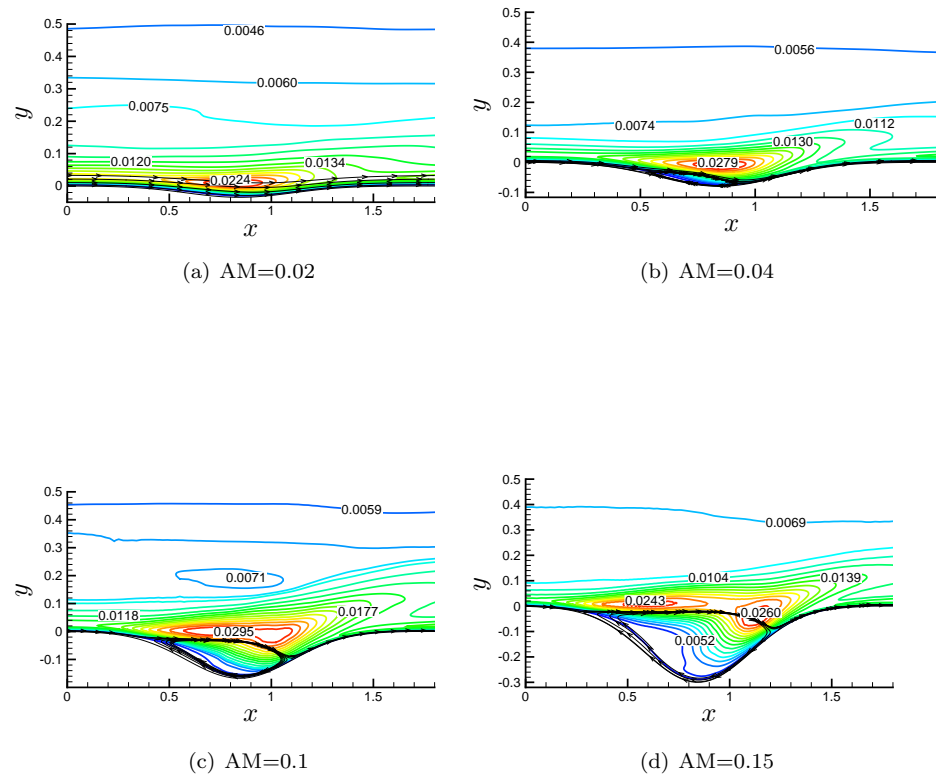


Figure 10: Contours of the time and spanwise averaged Reynolds stress component ($\langle u'^2 \rangle$) for different wave amplitudes (AM)

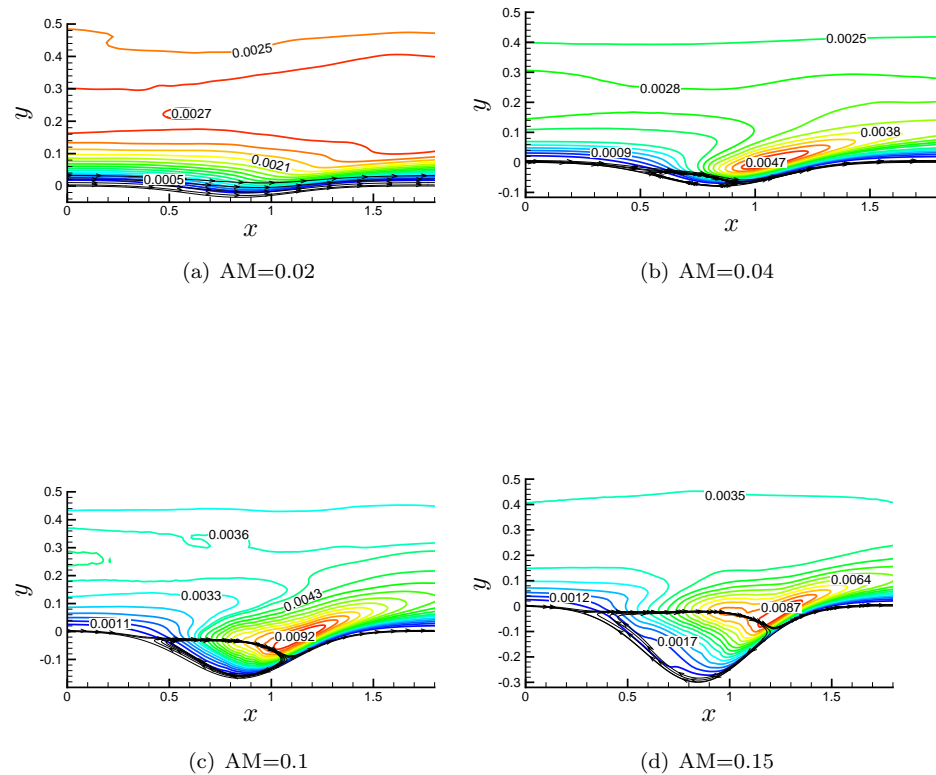


Figure 11: Contours of the time and spanwise averaged Reynolds stress component ($\langle v'^2 \rangle$) for different wave amplitudes (AM)

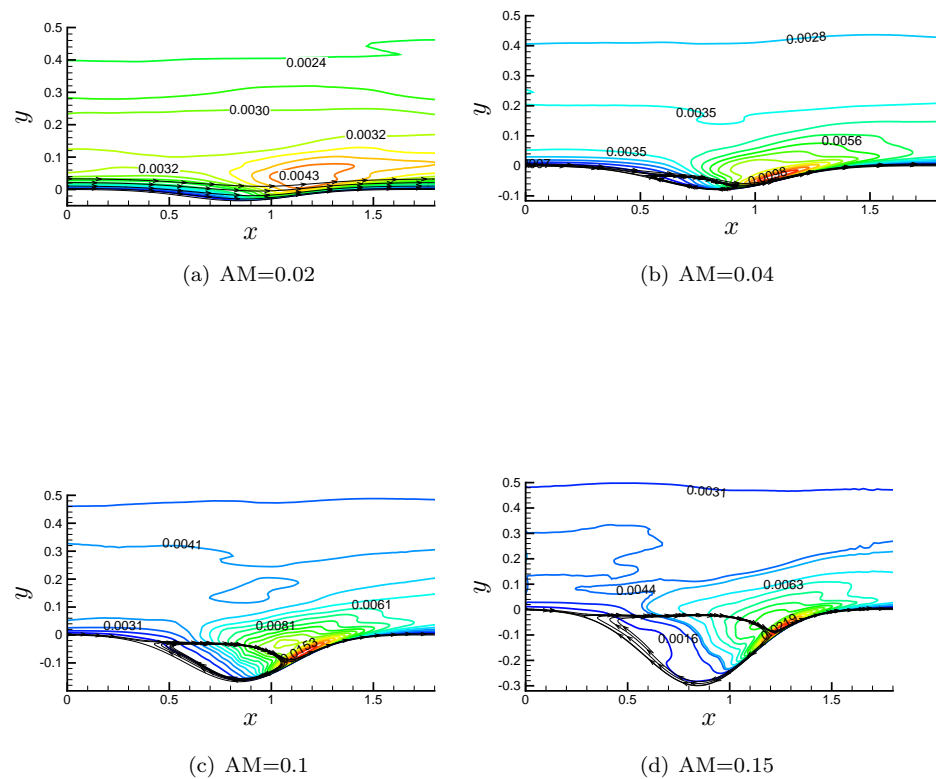


Figure 12: Contours of the time and spanwise averaged Reynolds stress component ($\langle w'^2 \rangle$) for different wave amplitudes (AM)

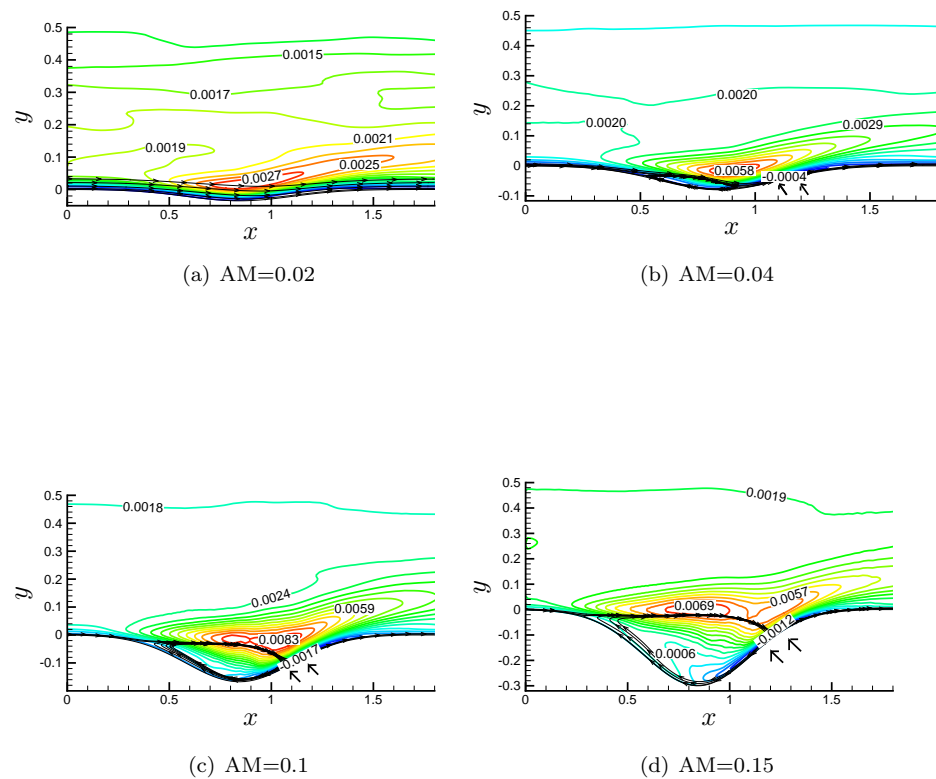


Figure 13: Contours of the time and spanwise averaged Reynolds stress component $(-\langle u'v' \rangle)$ for different wave amplitudes (AM)

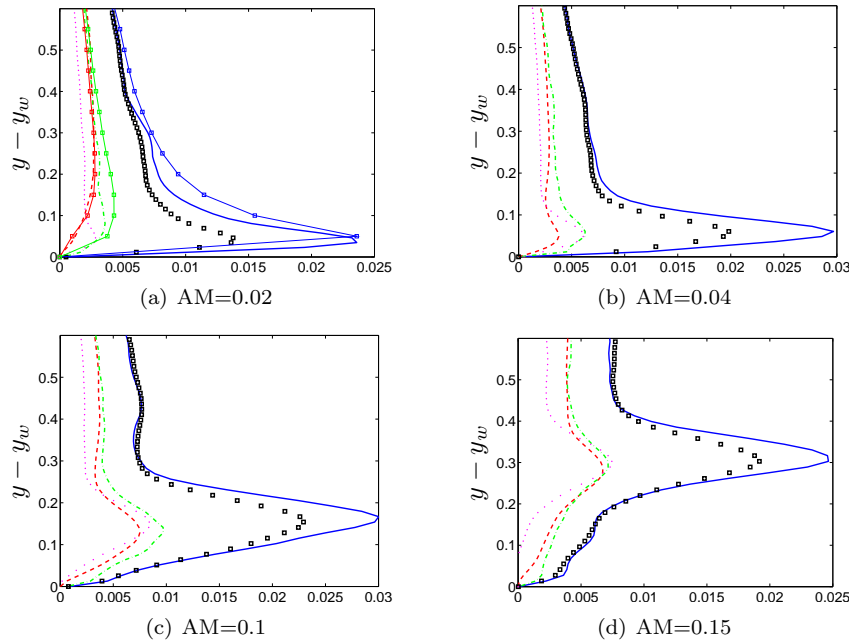


Figure 14: The wall-normal distributions of Reynolds stress components ($\langle u'^2 \rangle$, $\langle v'^2 \rangle$, $\langle w'^2 \rangle$, $-\langle u'v' \rangle$) and turbulent kinetic energy (k) for different wave amplitudes (AM) at the centre of the wave ($x = 0.8$), — : $\langle u'^2 \rangle$; - - - : $\langle v'^2 \rangle$; - - : $\langle w'^2 \rangle$; - - - : $-\langle u'v' \rangle$; \square : k ; lines with markers in $AM = 0.02$ present the *DNS* results of plane channel ($AM = 0$).

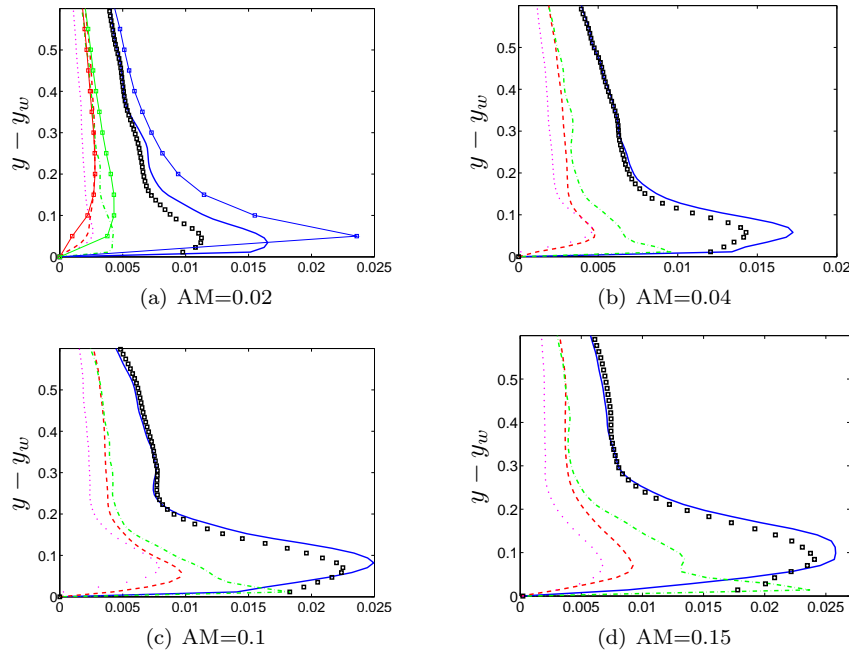


Figure 15: The wall-normal distributions of Reynolds stress components ($\langle u'^2 \rangle$, $\langle v'^2 \rangle$, $\langle w'^2 \rangle$, $-\langle u'v' \rangle$) and turbulent kinetic energy (k) for different wave amplitudes (AM) at the cross section close to the reattachment point, $x = 1.2$.
—: $\langle u'^2 \rangle$; --: $\langle v'^2 \rangle$; ---: $\langle w'^2 \rangle$; ...: $-\langle u'v' \rangle$; □: k ; lines with markers in $AM = 0.02$ present the *DNS* results of plane channel ($AM = 0$).

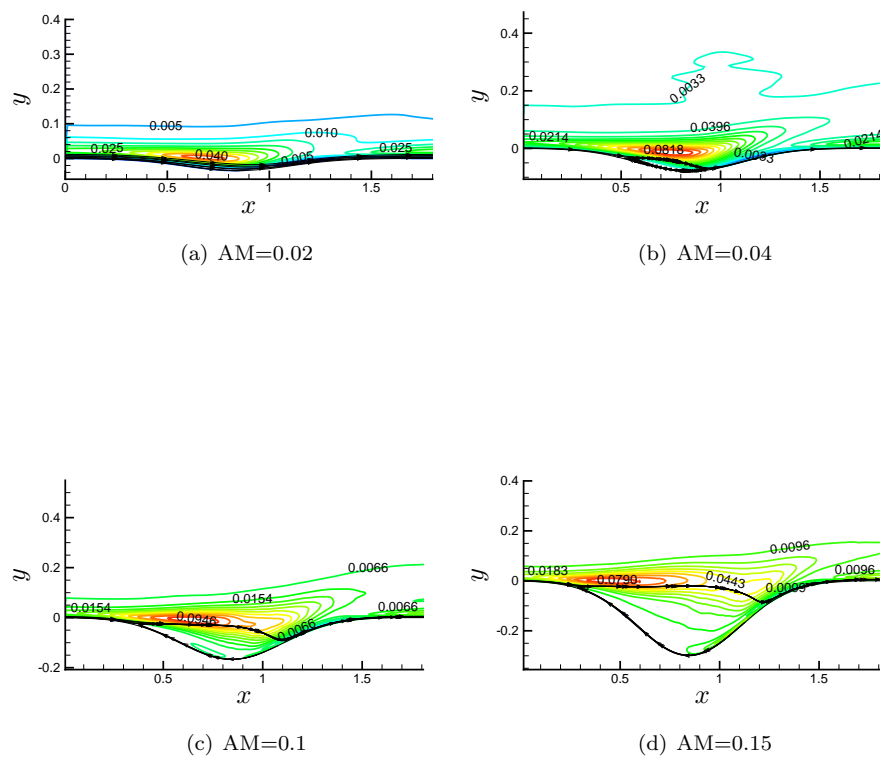


Figure 16: Contours of the time and spanwise averaged production of $\langle u'^2 \rangle$ (P_{11}) for different wave amplitudes (AM)

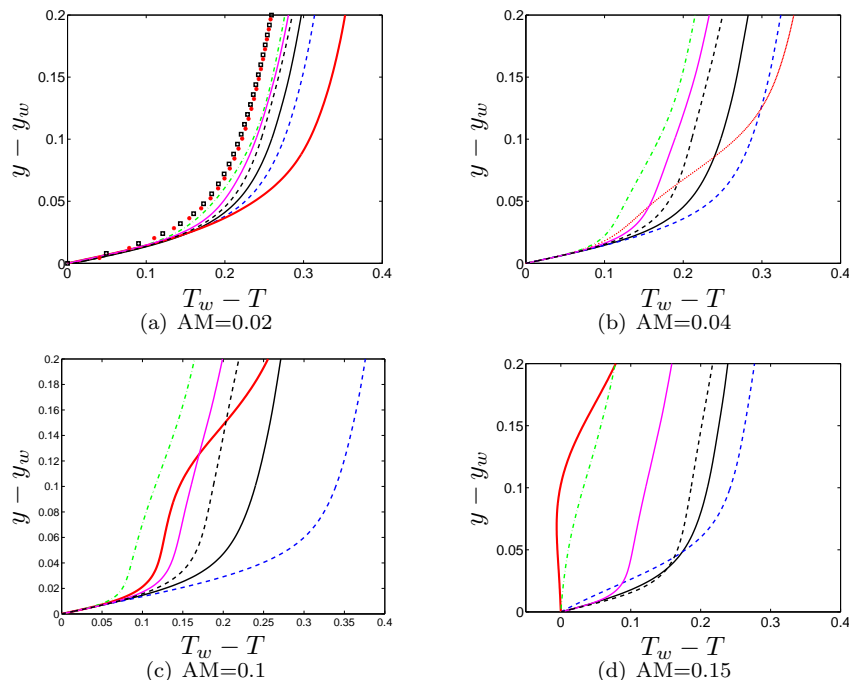


Figure 17: Wall-normal distributions of the time and spanwise averaged temperature ($T_w - T$) for different cross sections. The cross sections are shown in figure 1, — : $x = 0.2$; - - - : $x = 0.4$; — : $x = 0.8$; - · - : $x = 1.2$; — : $x = 1.6$; - - - : $x = 2$; \square : DNS [17]; \cdots : DNS present study.

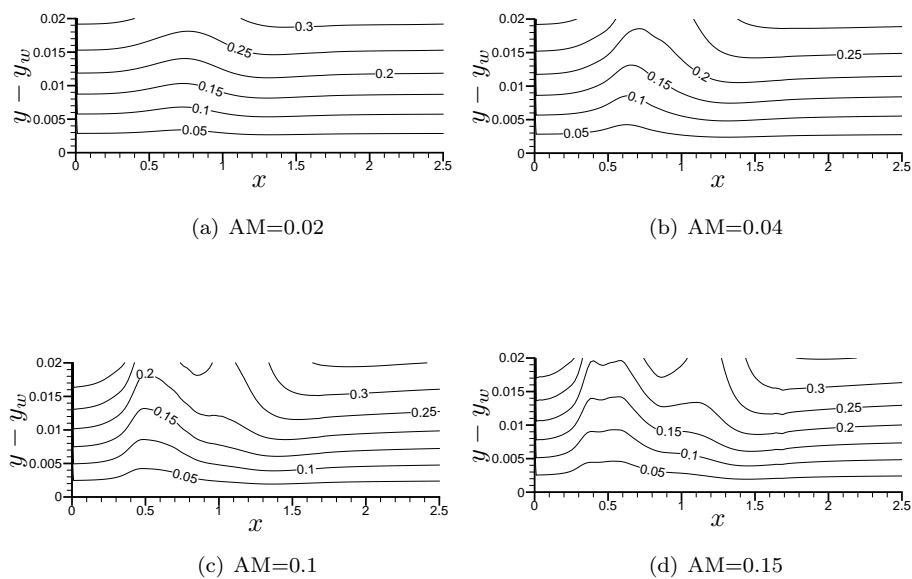


Figure 18: Contours of thickness of the thermal boundary layer (δ_T) in the wavy part of the channel for different wave amplitudes (AM)

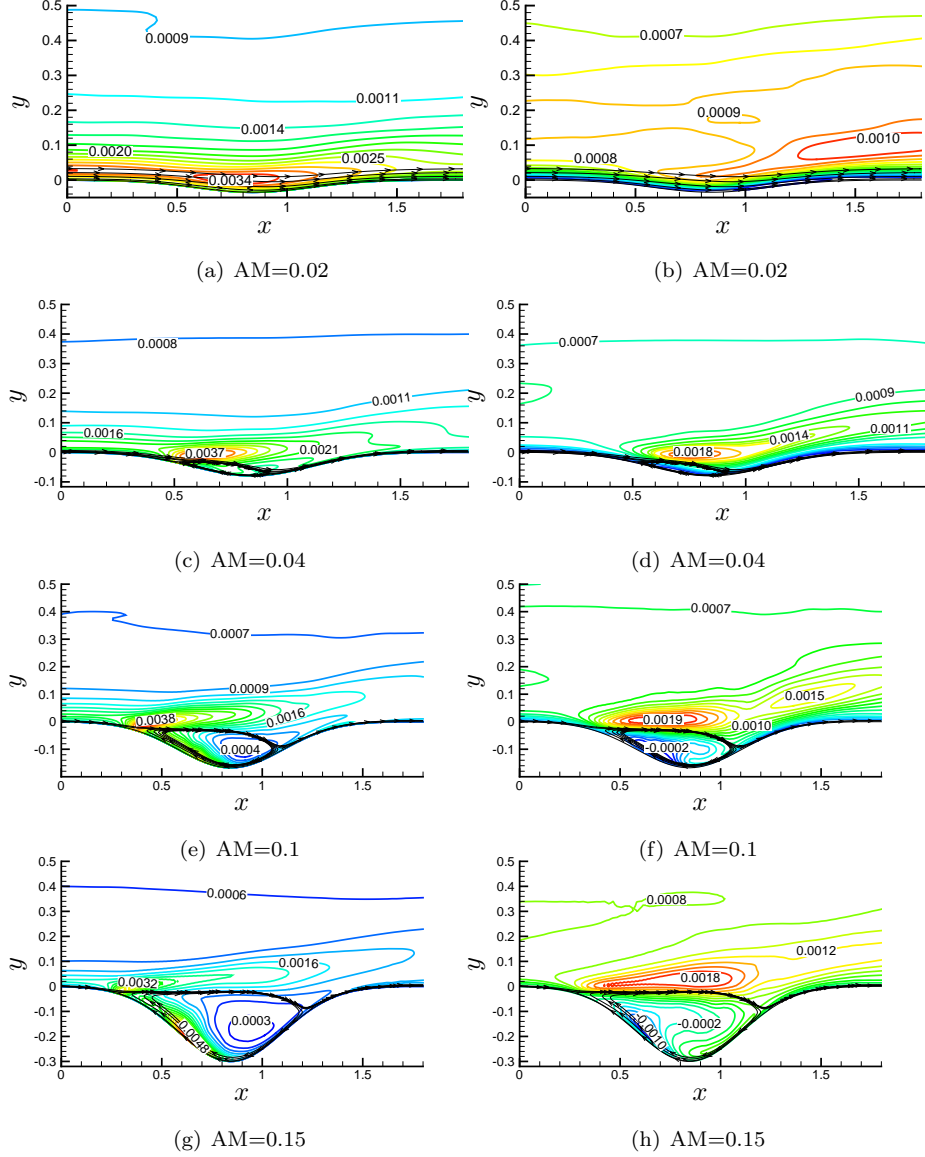


Figure 19: Contours of time and spanwise averaged wall-normal turbulent heat transfer, $\langle v't' \rangle$, (right side) and temperature fluctuations, t_{rms} , (left side) for different wave amplitudes (AM)

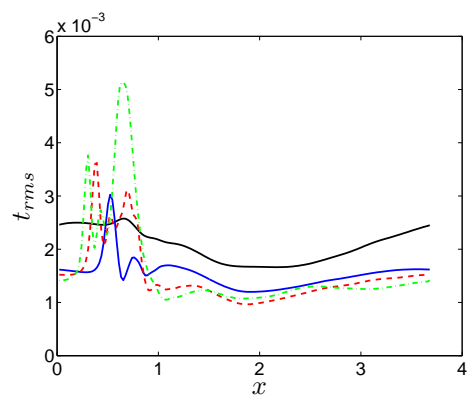


Figure 20: Streamwise variation of the time and spanwise averaged temperature fluctuation (t_{rms}) at the wall in the wavy part of the channel, — : $AM = 0.02$; — : $AM = 0.04$; - - : $AM = 0.1$; - · - : $AM = 0.15$

8 Corrections

Reviewer 1

Comments:

1. Reviewer's comment: "*The configuration exhibits only one corrugation with a long flat section downstream, which would make it of minor practical interest ...*".

As mentioned in page 4, the periodic boundary condition is used in the streamwise direction and the configuration (one corrugation with a flat section, see figure 1) is part of a corrugated channel with infinite numbers of the chosen half-corrugated channel. The selected geometry is part of the periodic half-corrugated channel used in Tetra Pak. This point has been added to page 3.

2. Reviewer's comment: "*There is little analysis of the physical mechanisms causing e.g. the increase of heat transfer in the reattachment region. The paper could be improved if such an analysis would be added.*".

The text "The maximum values of Nu and C_f are located at ... Further detailed discussions can also be found in [4] and [11]." has been added to the last part of the second paragraph of page 8.

3. Reviewer's comment: "*The procedure how Nu is extracted from the LES data should be explained.*".

The text "The bulk velocity and temperature are ..." and "The Nusselt number is defined as ..." have been added to the last part of the first paragraph of page 6.

4. Nu/Nu_0 column, showing the increase of heat transfer per total surface area, has been added to Table 2. The manuscript has been modified in page 9.

5. A list of symbols has been added in page 13 .

Style and language recommendations

1. Page 3: "until a critical" has been changed to "until a critical value".
2. Page 3: "In previous" has been changed to "In a previous".
3. Page 3: The last sentence of the first paragraph has been replaced by "The reduced magnitude between $x = 0$ and the separation point is almost the same and about 40% while, between the reattachment point and the end of the pitch, the increase is 21% and 36% for $Pr = 0.71$ and 3.5, respectively [11]."

4. Page 5: g_{ij} has been explained in list of symbols.
5. Page 7: "are closely predicted" has been changed to "are closely reproduced".
6. Page 7: "is too small and no separation occurs" has been changed to "is too small for a separation to occur".
7. Page 7: "By attention to" has been changed to "Inspecting".
8. Page 26: Figure 13 has been placed before figures 14 and 15. $u'v'$ has been added to figures 14 and 15. The manuscript has been modified in pages 10-11.
9. Page 10: "the largest effect" has been changed to "the largest relative effect".
10. Page 11: "are also present" has been changed to "are also presented".
11. Page 11: "are almost similar" has been changed to "are quite similar".
12. Page 11: "a ource term" has been changed to "a source term".
13. Page 11: "that similar" has been changed to "that a similar".
14. Page 11: "on thermal field" has been changed to "on the thermal field".
15. Conclusion, page 13: "the maximum and minimum locations of ..." has been changed to "the minimum and maximum locations of ...".
16. Page 32, figure 20: t_{rms} for all AM's has been shown. The manuscript has been modified in page 12.
17. Page 13: "high turbulent" has been changed to "highly turbulent".

Reviewer 3

1. Page 4, Eqs. 1: β and γ have been defined in the first paragraph after Eqs. 1. They have been also explained in the list of symbols.
2. Page 6: A uniform grid resolution was chosen for both the streamwise and spanwise directions in all the grids. This point has been added to page 6 of the manuscript.
3. Figures 8 and 14: All the legends have been explained for each figures.
4. The referee has mentioned that: "*In figure 14 The DNS results of the present study for the plane channel are also presented. For case of $AM = 0.02$ and 0.04 , stream-wise fluctuations are higher as compared to $AM = 0$ (DNS results) as indicated in figure 14. This needs to be addressed. It would be good if authors explain the reason of increase in fluctuations at small AM ratios compared to high AM ratios.*"
The text "The maximum value of $\overline{u'^2}$ increases by increasing the ... This explains the variation of $\overline{u'^2}$ with wave amplitude." has been added to the last part of the second paragraph of page 11. Figure 16, showing the production of $\overline{u'^2}$, P_{11} , has been added which explains the variation of $\overline{u'^2}$ with wave amplitude.
5. Page 11: Some explanations about the variations of k has been added to the second paragraph.